

Efficient 3D Perception on Embedded Systems via Interpolation-Free Tri-Plane Lifting and Volume Fusion

Sibaek Lee, Jiung Yeon and Hyeonwoo Yu

Abstract—Dense 3D convolutions provide high accuracy for perception but are too computationally expensive for real-time robotic systems. Existing tri-plane methods rely on 2D image features with interpolation, point-wise queries, and implicit MLPs, which makes them computationally heavy and unsuitable for embedded 3D inference. As an alternative, we propose a novel interpolation-free tri-plane lifting and volumetric fusion framework, that directly projects 3D voxels into plane features and reconstructs a feature volume through broadcast and summation. This shifts nonlinearity to 2D convolutions, reducing complexity while remaining fully parallelizable. To capture global context, we add a low-resolution volumetric branch fused with the lifted features through a lightweight integration layer, yielding a design that is both efficient and end-to-end GPU-accelerated. To validate the effectiveness of the proposed method, we conduct experiments on classification, completion, segmentation, and detection, and we map the trade-off between efficiency and accuracy across tasks. Results show that classification and completion retain or improve accuracy, while segmentation and detection trade modest drops in accuracy for significant computational savings. On-device benchmarks on an NVIDIA Jetson Orin nano confirm robust real-time throughput, demonstrating the suitability of the approach for embedded robotic perception.

I. INTRODUCTION

Real-time, precise 3D perception enables robots to accurately localize themselves, detect and avoid obstacles, and manipulate objects reliably in dynamic environments, as shown in Figure 1. However, as voxel resolution increases, this cubic growth in computational complexity and memory usage quickly exceeds the limits of onboard embedded systems, making real-time processing impossible [1], [2]. To address these challenges, methods typically exploit spatial sparsity or project 3D volumes onto 2D planes. Sparse convolution techniques [3], [4] selectively perform computation only on non-empty voxel locations, thereby avoiding wasted operations in unoccupied space. Approaches such as MinkowskiNet [5] focus processing on non-empty regions, but they remain computationally expensive due to their reliance on 3D convolutions and face performance overheads. While this sparsity accelerates binary occupancy inputs, its advantage vanishes on continuous-density fields, where most voxels carry nonzero values. Projection-based methods [6], [7], [8], [9] construct an axis-aligned tri-plane representation from 2D image features or latent volumes, and then interpolate features from the three planes to query

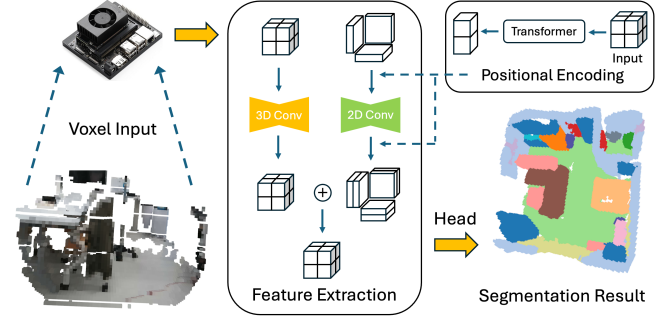


Fig. 1. Real-time 3D Perception on Embedded Systems. Our approach aims to perform real-time 3D perception tasks on general 3D voxel inputs within an embedded environment. This figure illustrates our efficient hybrid design, which fuses 2D and 3D convolutional streams and includes a lightweight positional encoding module to enhance geometric detail.

arbitrary 3D points. These features are typically processed by implicit MLPs for downstream 3D tasks, such as generative scene synthesis or occupancy prediction. While this scheme leverages the efficiency of 2D convolutions, it still depends on point-wise queries and interpolation, leading to high computational overhead and making it less suitable for real-time embedded reasoning.

In this work, we revisit the tri-plane representation as a lightweight backbone for efficient 3D voxel reasoning. Unlike prior approaches that mainly applied tri-planes for generative modeling or occupancy prediction, our design explicitly targets real-time inference on embedded robotic systems. We propose an interpolation-free lifting scheme that derives feature tri-planes from voxel projections with 2D convolutions, and restores a 3D feature volume via broadcast and summation. This design removes the need for interpolation, point-wise queries, and implicit MLPs, thereby reducing complexity. We further strengthen this backbone by adding a low-resolution volumetric branch and integrating it with the lifted features through a lightweight channel-mixing step. This hybrid design preserves coarse global context while maintaining an end-to-end GPU accelerated structure, enabling both efficiency and accuracy gains over interpolation-based tri-plane methods. In addition, we include an adaptive positional encoding as an auxiliary modulation. Unlike fixed sinusoidal encodings [10] or voxel-wise MLPs [11], our module generates adaptive embeddings that capture inter-slice relationships. Because its computational overhead is negligible (less than 0.1% of the backbone’s FLOPs), it provides an economical way to enhance reconstruction fidelity by recovering fine geometric detail, complementing the efficiency-oriented backbone design.

Sibaek Lee, Jiung Yeon and Hyeonwoo Yu are with the Department of Intelligent Robotics, Sungkyunkwan University, Suwon, South Korea. {lmj1ss, wcr12st, hwyu}@g.skku.edu

The code is available at: <https://github.com/Lab-of-AI-and-Robotics/E3D-Perception>

We evaluate our method on a diverse set of 3D vision tasks, including shape classification and completion on ModelNet40 [12], semantic segmentation on ScanNet [13] and Stanford3D [14], and object detection on Hypersim [15], 3D-FRONT [16], and ScanNet. The results show that classification and completion retain or improve accuracy while for segmentation and detection, the method shows a favorable trade-off, exchanging modest accuracy for large computational savings. In all tasks, our method achieves substantial reductions in theoretical GFLOPs and improvements in measured on-device FPS compared to dense and sparse convolution baselines, demonstrating efficiency gains that enable real-time deployment. This confirms that our approach does not simply optimize accuracy, but instead maps the efficiency–accuracy trade-off across different tasks, which is critical for embedded robotic perception. On-device benchmarks on an NVIDIA Jetson Orin nano further validate real-time throughput, supporting the practical relevance of the proposed design. We summarize our main contributions as follows:

- An interpolation-free tri-plane lifting pipeline that eliminates interpolation, point-wise queries, and implicit MLPs, establishing tri-planes as a practical backbone for 3D voxel reasoning.
- A hybrid architecture that integrates our lifting backbone with a low-resolution volumetric branch and an auxiliary positional encoding module. This design effectively preserves global context and recovers fine details with negligible overhead while maintaining end-to-end GPU parallelism.
- A systematic efficiency–accuracy trade-off analysis across classification, completion, segmentation, and detection, clarifying when accuracy can be preserved and when efficiency gains justify modest losses.
- On-device validation on Jetson Orin nano, confirming real-time throughput and demonstrating practical suitability for embedded robotic perception.

II. RELATED WORK

Dense 3D convolution is highly expressive but its computational and memory costs scale cubically with voxel resolution. To mitigate this, submanifold and sparse convolutions along with MinkowskiNet confine computation exclusively to active, non-empty voxels, yielding substantial computational savings, particularly in environments with low occupancy [3], [4], [5]. Later works continued to reduce redundancy and latency. SPS-Conv [17] prunes uninformative sites, VoxelNeXt [18] builds fully sparse backbones, and SparseOcc [19] maintains fully sparse latent volumes without loss of accuracy. Yet these methods still use 3D kernels and add nontrivial overhead.

Orthogonal to sparsity, projection-based methods replace volumetric 3D convolution with 2D convolution after mapping 3D structure onto planar grids. Representative methods include OFT [20] for monocular lifting to an orthographic space, PointPillars [21], which evolved from early sparse convolutional detectors like SECOND [22], for pillarized

pseudo images, RangeNet++[23] for range view segmentation, and Lift, Splat, Shoot[24] for multi-camera lifting to BEV, later extended by transformer-based methods such as BEVFormer [25]. More recently, EG3D [6] demonstrated that tri-plane features can support generative rendering, where features are interpolated from the planes and decoded by implicit MLPs. Triplane Diffusion [7] scaled this idea to diffusion-based 3D neural field generation, while SemCity [8] and TPVFormer [9] adapted tri-planes for semantic scene synthesis and occupancy prediction, respectively. Although these methods show the versatility of tri-plane structures, they all rely on interpolation and point-wise queries coupled with implicit decoders, which introduce irregular memory access and limit real-time feasibility. In contrast, our design employs an interpolation-free broadcast-summation to directly reconstruct voxel features, enabling dense GPU-parallel execution and making it better suited for real-time 3D reasoning. In contrast, our approach starts directly from voxel inputs and reconstructs the feature volume without interpolation, distinguishing it from EG3D and related tri-plane methods that rely on image-space features and point-wise queries.

Projection-based pipelines collapse a 3D structure onto a set of 2D planes, a process that invariably discards critical spatial cues. Since tiling per-plane features back into 3D does not recover them, models inject positional information. Fixed encodings include sinusoidal mappings in Transformers [26], coordinate channels [10], and Fourier features [27], which are effective for high-frequency 3D representation learning [28].

Learned variants extend this idea by adapting positional features from data, such as relative coordinate encodings in point clouds (Point Transformer [29]) and discrete voxel embeddings (Voxel Transformer [30]). Multi-view detection frameworks further map 3D coordinates to embeddings with lightweight MLPs, as in PETR [11]. These approaches highlight the importance of positional cues for mitigating projection-induced losses, but they typically treat positional encoding as a central modeling component. In contrast, our method introduces an adaptive positional encoding as an auxiliary signal to strengthen interpolation-free tri-plane lifting.

III. METHOD

We propose an efficient hybrid architecture to address the high computational cost of dense 3D convolutions. In the following subsections, we first detail our core interpolation-free tri-plane lifting framework, which includes an adaptive positional modulation to retain spatial detail (Section III-A). We then describe the parallel low-resolution volumetric branch used for capturing global context (Section III-B). Finally, we explain how these two streams are merged through a lightweight fusion module to produce the final representation (Section III-C).

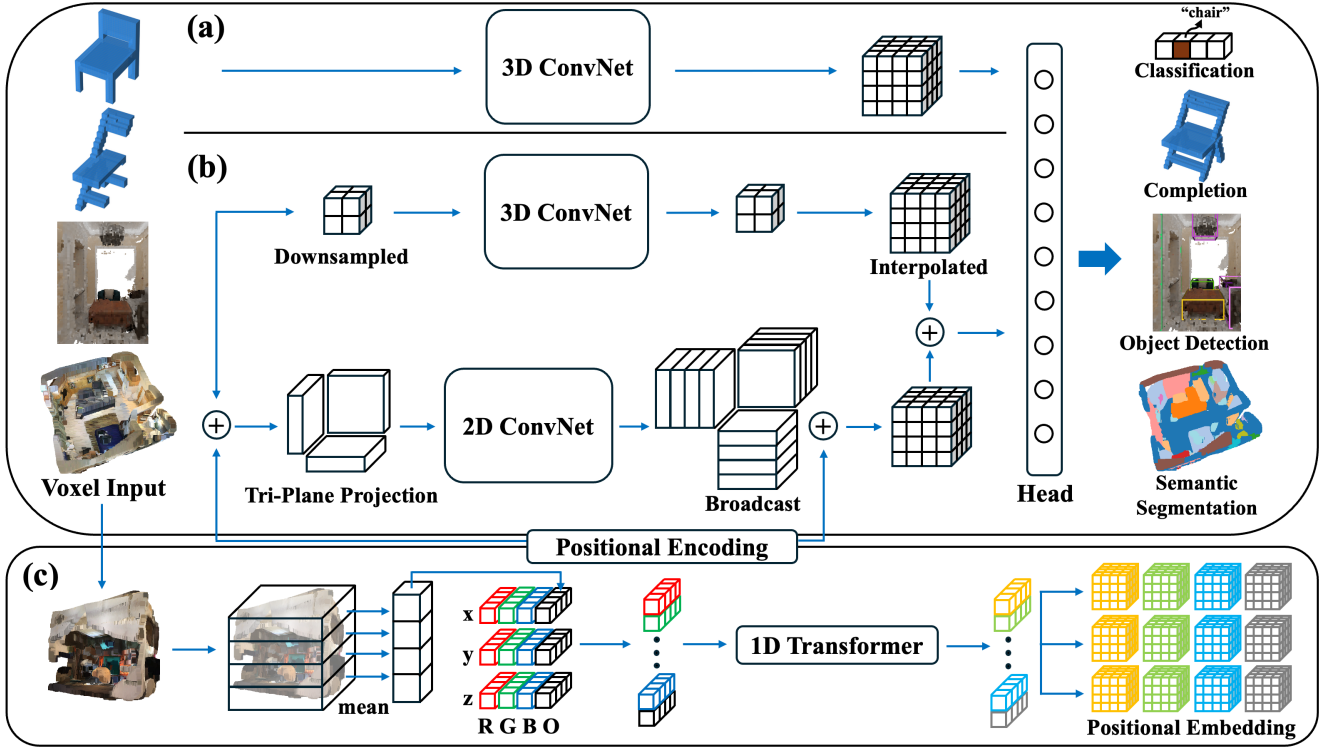


Fig. 2. System Overview. (a) A dense 3D ConvNet baseline. (b) Our efficient hybrid architecture, which fuses a fast tri-plane 2D stream with a coarse 3D stream; the latter processes a downsampled volume and interpolates the features back to the original resolution. (c) The generation process of our data-adaptive positional encoding. The 3D input is summarized into 1D tokens, which a transformer processes to create dynamic positional embeddings. These embeddings act as an information bridge to retain spatial details in our pipeline.

A. Interpolation-Free Tri-Plane Lifting

The core of our approach is an interpolation-free lifting pipeline that constructs a 3D feature volume from 2D plane projections. This design shifts the main computational load to lightweight 2D convolutions, ensuring high efficiency and real-time performance. Figure 2a shows the dense 3D CNN baseline, whose full-resolution convolutions incur heavy FLOPs and memory, while Figure 2b presents our proposed hybrid approach.

For the input volume $V \in \mathbb{R}^{D_x \times D_y \times D_z}$, we create three orthogonal average projections, one for each primary axis $k \in \{x, y, z\}$, according to the following formula:

$$P_k(u, v) = \frac{1}{D_k} \sum_{d=1}^{D_k} V_k(u, v, d). \quad (1)$$

Each plane P_k is processed by a lightweight 2D CNN g_k to produce a feature map $F_k = g_k(P_k)$. We then lift these plane features back to 3D by broadcasting them along the missing dimension:

$$\hat{F}_i(u, v, w) = F_i(u, v), \text{ where } i = x, y, z. \quad (2)$$

The lifted feature volume T is then obtained as a weighted combination of the three tensors:

$$T = \lambda_x \hat{F}_x + \lambda_y \hat{F}_y + \lambda_z \hat{F}_z \quad (3)$$

where $\lambda_x, \lambda_y, \lambda_z$ are learnable coefficients that adaptively balance contributions from each plane. Unlike prior tri-plane

methods that rely on point-wise interpolation and implicit MLPs, our broadcast-summation scheme constructs the feature volume in one step, reducing the operation to dense element-wise additions that map efficiently to GPU kernels. This makes the process fully parallelizable, avoids irregular memory access, and scales linearly with voxel resolution rather than cubically as in dense 3D convolutions.

Projecting the 3D volume onto planes inevitably removes fine voxel-level relations, and simple broadcast-summation cannot fully recover them. To compensate, we introduce an *adaptive positional modulation* that supplements broadcast-addition with global spatial cues. A lightweight transformer summarizes the input volume $V \in \mathbb{R}^{C \times D_x \times D_y \times D_z}$ by average projections along the x, y, z axes, producing token sequences $\mathbf{t}_{c,k}$. For example, the x -axis token is

$$\mathbf{t}_{c,x}[i] = \frac{1}{D_y D_z} \sum_{j=1}^{D_y} \sum_{l=1}^{D_z} V_{c,ijl}. \quad (4)$$

These tokens are processed to generate axis-conditioned embeddings $E = \{\mathbf{e}_{c,k}\}$, which act as weighting functions providing coarse global context.

The embeddings are applied as an additive bias in two stages. First, for pre-modulation, a weight volume W_{pre} is generated from the embeddings and added to the input volume before projection:

$$V'_c(i, j, k) = V_c(i, j, k) + W_{pre}(i, j, k). \quad (5)$$

Second, for post-modulation, another weight volume W_{post} is generated to refine the lifted volume T after reconstruction, yielding the final volume $T' = T + W_{post}$. This two-stage modulation re-injects spatial cues with negligible overhead (<0.1% FLOPs).

B. Low-resolution Feature Volume

In parallel, we downsample the input volume \tilde{V} with ratio r and process it with a compact 3D CNN h to capture coarse global context. The result is then upsampled to the original resolution to form the volumetric feature G . This auxiliary pathway serves as a low-resolution volumetric branch. Following the memory-efficient design of MeRF [31], it applies 3D convolutions only on a reduced representation, minimizing overhead while retaining structural context.

Beyond efficiency, the low-resolution volumetric branch fulfills two key roles. First, it stabilizes training by injecting coarse structural cues that regularize the finer but noisier features of the lifted stream. Second, it reintroduces volumetric consistency that compensates for projection-induced information loss. Even at reduced resolution, this branch preserves long-range spatial correlations that are difficult to capture through tri-plane lifting alone, making it an essential complement to the broadcast-summation pathway.

C. Module Fusion

For fusing the lifted feature volume T and volumetric features G , we opt for element-wise summation over concatenation, in order to avoid increasing channel depth. This simple fusion achieves comparable performance to concatenation while minimizing overhead. While broadcast-summation alone can serve as the final fusion step, it limits representational flexibility. To enrich the combined features without introducing heavy computation, motivated by [32], [33], we apply a $1 \times 1 \times 1$ convolution block ϕ , which provides an efficient nonlinear channel adjustment while preserving end-to-end GPU parallelism. In our setting, it refines fused features without expanding spatial dimensions, keeping the operation lightweight while enhancing representational flexibility. The output prediction \hat{Y} is then obtained as:

$$\hat{Y} = \phi(T + G). \quad (6)$$

Consequently, the two streams T and G are fused by element-wise summation and refined through a lightweight $1 \times 1 \times 1$ convolutional block, producing a compact yet expressive representation. The resulting volume is then passed to the downstream task-specific head for classification, completion, segmentation, or object detection.

IV. EXPERIMENTS

We evaluate our proposed architecture across multiple 3D vision tasks to assess the efficiency–accuracy trade-offs of interpolation-free tri-plane lifting. Section IV-A describes the experimental setup, including datasets and evaluation metrics. Section IV-B reports comparative results against baseline methods on four tasks: classification, completion,

semantic segmentation, and object detection. Section IV-C presents ablation studies that examine the role of each design component, including the auxiliary positional encoding module. Section IV-D measures on-device throughput on an NVIDIA Jetson Orin nano to evaluate the method’s suitability for embedded deployment.

A. Experimental Setup

1) *Datasets and Evaluation Metrics:* We evaluate our method on four 3D vision tasks: shape classification, shape completion, semantic segmentation, and object detection. For shape classification and completion, we use the ModelNet40 [12] dataset. For semantic segmentation, we benchmark on two large-scale indoor scene datasets, ScanNet [13] and Stanford 3D [14]. For our 3D object detection experiments, we use the same datasets as NeRF-RPN [34]: Hypersim [15], 3D-FRONT [16], and ScanNet [13]. For all tasks, we preprocess the raw data by converting it into a volumetric voxel grid representation. The grid resolution is set to 128^3 for ModelNet40, ScanNet, and Stanford 3D. For the object detection datasets, we use a resolution of 160^3 for 3D-FRONT and ScanNet, and 200^3 for Hypersim to accommodate the varying scene scales.

We employ task-specific metrics for performance evaluation. For classification, we report accuracy (Acc), F-score, and Area Under the Curve (AUC). For completion, performance is measured by L2 Chamfer distance, F-score, and Intersection over Union (IoU). In semantic segmentation, we use mean IoU (mIoU), accuracy, and F-score. Finally, for object detection, we report Recall (R) and Average Precision (AP) at IoU thresholds of 0.25 and 0.50.

2) *Implementation Details and Comparisons:* Our approach builds on an interpolation-free lifting backbone. We denote this minimal variant as *Ours-B* (backbone), which projects the input volume onto three orthogonal planes, applies lightweight 2D convolutions, and restores the 3D feature volume via broadcast-summation. To assess the impact of auxiliary components, we further report *Ours-F* (Full), which augments the backbone with adaptive positional encoding (*PE*), a low-resolution volumetric branch (*Vol*), and a $1 \times 1 \times 1$ channel mixer. We also evaluate variants, denoted as *Ours-F*(r), where the volumetric branch processes an input downsampled by a ratio of r , to illustrate the efficiency–accuracy trade-off. For ablations, we define *Ours-F*(*NoPE*) as the full model without *PE*, and *Ours-F*(*var*) as versions where *PE* is replaced by sinusoidal, coordinate, or MLP encodings. These comparisons allow us to quantify the role of each component and to demonstrate that the full variant achieves the best trade-off among accuracy, efficiency, and real-time feasibility.

We compare our proposed architecture with other representative baselines. The first is a *3D Base* model, which represents a standard dense 3D convolutional neural network using a U-Net-like architecture. It processes the entire voxel grid and serves as a benchmark for maximum expressive power at a high computational cost. The second baseline is *3D Sparse*, which is designed to exploit the inherent spatial

TABLE I

3D CLASSIFICATION PERFORMANCE COMPARISON ON MODELNET40

Method	GFLOPs	Acc	F-score	AUC
3D Base	29.38	83.94	75.74	0.9871
3D Sparse	6.34	83.54	74.92	0.9877
<i>Ours-B</i>	0.96	82.52	75.86	0.9857
<i>Ours-F(1/2)</i>	4.42	82.93	75.81	0.9844
<i>Ours-F(1/4)</i>	1.34	83.54	76.60	0.9823

The **best** and **second-best** results are highlighted.

TABLE II

3D COMPLETION PERFORMANCE COMPARISON ON MODELNET40

Method	GFLOPs	L2 Chamfer	F-score	IoU
3D Base	78.61	0.001421	70.87	56.22
3D Sparse	29.52	0.002205	66.27	50.20
<i>Ours-B</i>	2.05	0.012340	49.26	33.08
<i>Ours-F(1/2)</i>	12.28	0.001494	76.26	62.03
<i>Ours-F(1/4)</i>	3.59	0.001392	74.23	60.07

sparsity within 3D data by building on submanifold sparse convolutions, similar to methods like MinkowskiNet [5]. It restricts computations to active voxels to reduce FLOPs.

For the segmentation task, both streams utilize U-Net architectures to effectively handle dense prediction. For the other tasks of classification, completion, and object detection, we use standard feed-forward CNNs. All models were trained on a single NVIDIA RTX 4090 GPU.

B. Experiment Results and Analysis

Our experimental results demonstrate that our hybrid architecture achieves a balanced trade-off between computational efficiency and task performance. As illustrated in Figure 3, the models *Ours-F(1/2)* and *Ours-F(1/4)* consistently occupy favorable positions along the efficiency–accuracy spectrum. They retain or improve accuracy in tasks such as classification and completion while substantially reducing GFLOPs, and they show a trade-off with moderate performance drops in exchange for large computational savings. This outcome validates our design: interpolation-free lifting secures efficiency, while positional encoding serves as an auxiliary bridge that helps mitigate, though not completely eliminate, the information loss from projection.

A detailed analysis of the quantitative results demonstrates distinct advantages of our hybrid approach across the four tasks. The classification results in Table I show that performance differences between methods are minor, as the task does not strictly require complex 3D reasoning. This performance gap widens significantly in shape completion, detailed in Table II, where full 3D understanding is crucial. As visualized in Figure 3, our models occupy a superior position of high accuracy at low cost. *Ours-F(1/4)* surpasses the heavyweight *3D Base* model across all metrics, achieving an F-score of 74.23 and an IoU of 60.07, compared to the baseline’s scores of 70.87 and 56.22, respectively. We interpret this outcome not as a universal accuracy gain, but as an effect of the hybrid architecture acting as an information bottleneck, which provides a regularization-like benefit in this specific task. This process is enabled by our

TABLE III

3D SEMANTIC SEGMENTATION ON SCANNET AND STANFORD 3D

Method	GFLOPs	ScanNet			Stanford 3D		
		mIoU	Acc	F-score	mIoU	Acc	F-score
3D Base	540.18	40.21	74.68	60.34	51.63	84.14	68.47
3D Sparse	118.70	42.17	79.34	61.98	48.90	85.38	66.25
<i>Ours-B</i>	10.35	24.12	55.50	43.01	40.46	73.44	60.91
<i>Ours-F(1/2)</i>	87.21	34.19	70.50	54.62	50.53	82.18	68.28
<i>Ours-F(1/4)</i>	27.63	30.18	63.78	49.44	44.69	76.36	61.59

data-adaptive positional encoding, which effectively bridges the information lost during projection while keeping the representation compact, leading to favorable trade-offs in tasks that require strong geometric reasoning.

In semantic segmentation, the results in Table III highlight the efficiency-accuracy trade-offs of our approach. On the Stanford 3D dataset, *Ours-F(1/2)* model achieves an mIoU of 50.53, outperforming the 3D Sparse baseline (48.90) while operating at lower computational cost, and approaching the performance of the dense 3D Base model (51.63). These results suggest that even though projection-based lifting inevitably loses some voxel-level relationships, our data-adaptive positional encoding partially compensates for this loss and yields more competitive accuracy when the dataset structure is favorable. At the same time, the efficiency advantage of our method becomes particularly clear in object detection, where dense inputs reduce the benefit of sparse convolution. As shown in Table IV, the 3D Sparse model requires 1262.09 GFLOPs on Hypersim, close to the 1615.84 GFLOPs of the 3D Base, while *Ours-F(1/4)* operates at only 77.65 GFLOPs. Despite this drastic reduction, it delivers detection performance competitive with both baselines, confirming that our design consistently provides an effective trade-off between efficiency and accuracy.

We also provide a qualitative analysis in Figure 4 to visually assess our method’s performance. For shape completion, the limitations of projection-based methods are evident; the *Ours-B* baseline produces a sparse, incomplete artifact that fails to capture the object’s structure. While the *3D Base* and *3D Sparse* models generate more reasonable shapes, they struggle with fine details, leaving chair legs partially missing or distorted. In contrast, our method reconstructs a complete chair with all four legs, closely matching the ground truth geometry. This consistency is also observed in semantic segmentation. The *Ours-B* output is heavily fragmented, and even the *3D Base* and *3D Sparse* methods show noisy boundaries. As highlighted in the red dashed box on the left, other methods mis-segment the object, whereas our approach produces a cleaner map that aligns more closely with the ground truth. A similar pattern appears in object detection, where the other methods either miss certain objects or produce multiple inaccurate boxes for a single object, as highlighted by the red dashed boxes. Our method instead produces bounding boxes that are more consistent and better aligned with the ground truth. These visualizations collectively indicate that our architecture, despite its significantly lower computational cost, retains structural fidelity that is

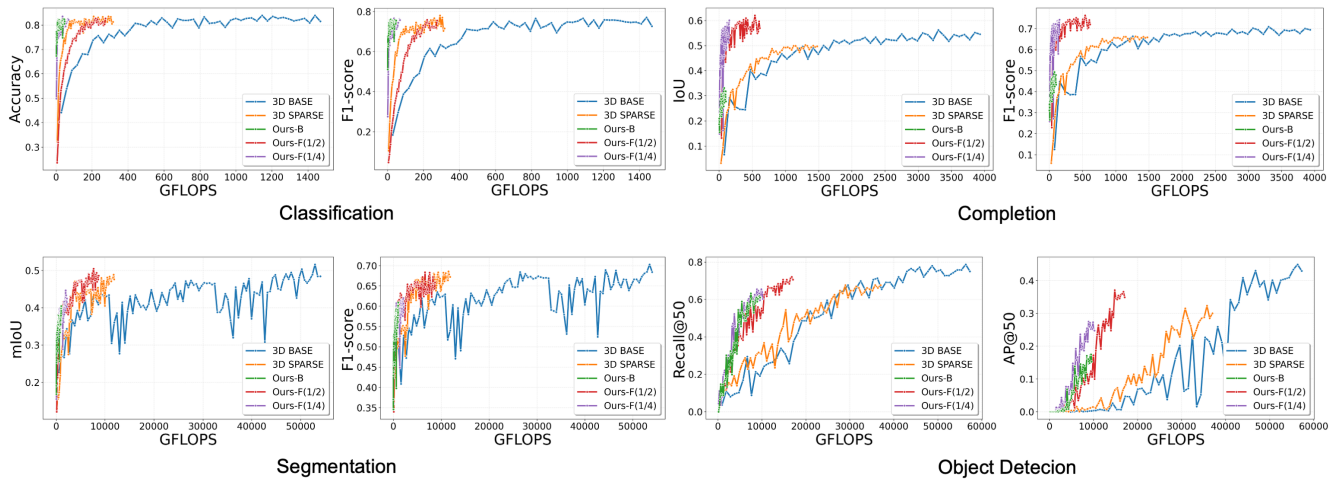


Fig. 3. Performance against computational cost across four 3D vision tasks. Our full models, *Ours-F(1/2)* and *Ours-F(1/4)*, achieve accuracy comparable to the computationally intensive *3D Base* and *3D Sparse* models at a fraction of the computational cost. The *Ours-B* variant highlights the efficiency of our core backbone, which provides a strong baseline. Notably, for the shape completion task, our approach surpasses the performance of all baseline methods.

TABLE IV
3D OBJECT DETECTION PERFORMANCE COMPARISON ACROSS 3D-FRONT, HYPERSIM, AND SCANNET

Method	3D-FRONT					Hypersim					ScanNet				
	FLOPs	R@25	R@50	A@25	A@50	FLOPs	R@25	R@50	A@25	A@50	FLOPs	R@25	R@50	A@25	A@50
3D Base	823.44	98.53	78.68	65.89	44.93	1615.84	65.40	25.71	14.16	4.04	823.44	89.16	42.36	38.47	10.51
3D Sparse	485.16	97.79	67.65	53.57	24.90	1262.09	54.33	13.33	5.33	0.68	395.44	82.37	26.69	16.87	1.55
<i>Ours-B</i>	28.21	94.85	63.24	31.86	11.91	44.44	52.02	11.38	3.29	0.48	28.21	81.77	22.17	19.36	1.35
<i>Ours-F(1/2)</i>	152.95	97.06	72.06	61.92	36.62	305.90	60.32	15.68	6.93	1.07	152.95	88.67	36.45	21.08	4.26
<i>Ours-F(1/4)</i>	38.82	95.59	65.44	55.20	27.46	77.65	53.06	13.97	5.82	0.58	38.82	85.71	30.05	18.55	2.01

FLOPs are reported in GFLOPs. R@25 and R@50 denote Recall, while A@25 and A@50 denote Average Precision, evaluated at IoU thresholds of 0.25 and 0.50, respectively. The reported FLOPs measure the 3D backbone and FPN. All methods share a common 3D RPN head, which adds a fixed computational cost of 131.58 GFLOPs for 3D-FRONT, 257.61 GFLOPs for Hypersim, and 131.58 GFLOPs for ScanNet.

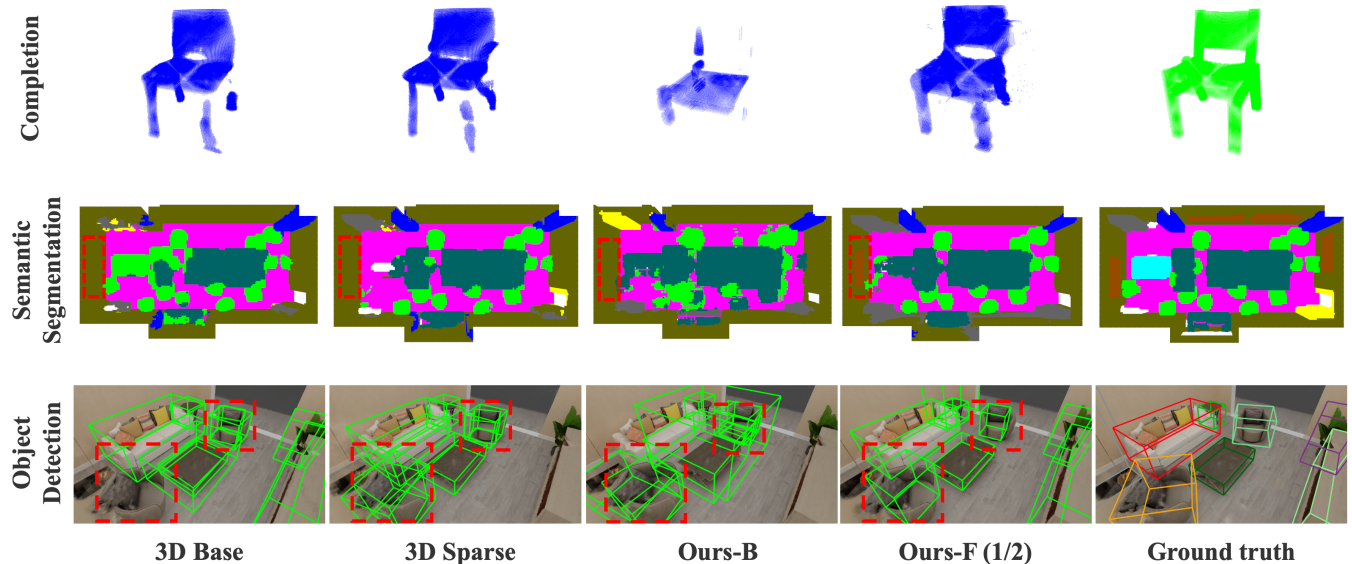


Fig. 4. Qualitative results for shape completion, semantic segmentation, and object detection. The visualization shows results for completion on ModelNet40 [12], semantic segmentation on Stanford3D [14], and object detection on 3D-FRONT [16]. Our full model, labeled *Ours-F(1/2)*, reconstructs a more complete shape in completion, while producing cleaner segmentation maps and more accurate bounding boxes than our backbone model, *Ours-B*. The visual quality is comparable to the more computationally expensive 3D methods.

often degraded in other approaches. For segmentation and object detection, the results reflect the expected trade-off between accuracy and efficiency, consistent with the intended design objective.

TABLE V
ABLATION STUDY OF POSITIONAL ENCODINGS AND ARCHITECTURES ACROSS TASKS AND DATASETS

Method	Classification	Completion	Semantic Segmentation		Object Detection		
	ModelNet	ModelNet	ScanNet	Stanford3D	Hypersim	3D-FRONT	ScanNet
<i>Ours-F(NoPE)</i>	74.55	74.38	53.70	65.41	70.12	14.60	33.53
<i>Ours-F(Sinusoidal)</i>	74.31	76.04	54.08	66.65	68.44	13.43	34.54
<i>Ours-F(CoordConv)</i>	74.42	74.39	53.38	66.11	68.38	13.73	34.47
<i>Ours-F(MLP)</i>	74.97	75.64	53.52	67.63	70.59	14.33	36.51
<i>Ours-F(Transformer)</i>	75.81	76.26	54.62	68.28	72.06	15.68	36.45

Performance is evaluated using the F1-score for classification, completion, and segmentation, and Recall@50 for object detection. All results are reported for the *Ours-F(1/2)* model configuration.

C. Positional Encoding Variants

Positional encoding introduces consistent accuracy gains across tasks at virtually no additional cost, with overheads below 0.1% of total FLOPs. These moderate improvements nonetheless represent an economical enhancement that reliably strengthens reconstructed features without compromising efficiency. Table V compares the full model (*Ours-F(1/2)*) with several variants: one without positional encoding, and others using fixed sinusoidal encoding [26], coordinate channels (CoordConv)[10], or a learned MLP[11]. Our transformer-based positional encoding module consists of a 2-layer Transformer Encoder with 8 attention heads and a model dimension of 128. The model without any positional encoding yields the lowest scores across nearly all metrics, such as an F1 of 74.38 in completion, indicating that bridging spatial information is important for counteracting the loss from projection and reconstruction. Introducing fixed encodings like *Sinusoidal* and *CoordConv* gives only marginal benefit, reflecting the limited expressiveness of static mappings. The learned *MLP* variant generally performs better, for instance reaching an F1 of 67.63 on Stanford3D, suggesting that learned embeddings provide more flexibility. The transformer-based encoding achieves the strongest results overall, such as 54.62 F1 on ScanNet segmentation compared to 53.52 for the MLP-based variant. These results show that context-aware positional signals generated by the transformer, which capture global structure and inter-slice relationships, consistently yield the most reliable improvements across tasks.

D. On-Device Performance Evaluation

To validate the practical applicability of our method for real-world robotics, we extend our analysis beyond theoretical FLOPs and measure the on-device inference speed. We deployed our models on the onboard NVIDIA Jetson Orin nano with a RealSense D435i depth camera. The results, reported as Frames Per Second (FPS) for each task, are summarized in Table VI. The on-device results confirm the efficiency of our hybrid approach. For instance, in the object detection (OD) task, *Ours-F(1/4)* achieves 6.09 FPS, compared to the 1.85 FPS of the 3D Base model. However, we observe that the measured FPS gains, while substantial, are not as pronounced as the theoretical GFLOPs reductions would suggest.

TABLE VI
ON-DEVICE FPS FOR EACH TASK ON NVIDIA JETSON ORIN NANO

Method	Cls.	Comp.	Seg.	OD
3D Base	14.20	11.28	1.53	1.85
<i>Ours-B</i>	49.58	35.79	10.87	10.64
<i>Ours-F(1/2)</i>	24.75	14.86	3.09	3.16
<i>Ours-F(1/4)</i>	45.93	17.52	4.01	6.09

Cls., Comp., Seg., and OD stand for Classification, Completion, Segmentation, and Object Detection, respectively.

This discrepancy is largely due to the system becoming memory-bound on the resource-constrained hardware. In addition, the backbone variant (*Ours-B*) runs faster than 3D Base, but without the positional encoding and volumetric branch its accuracy is limited, highlighting the necessity of the full model for practical deployment. The latency of memory access for reading and writing 3D voxel data can become a dominant bottleneck, limiting the real-world speedup regardless of the model’s computational cost. Furthermore, our current implementation processes the tri-plane and volumetric streams sequentially. This presents a clear opportunity for future optimization; by implementing parallel processing for these streams, the throughput could be further improved, better leveraging the multi-core capabilities of embedded processors.

V. CONCLUSION

In this work, we addressed the fundamental challenge of balancing computational cost and accuracy in 3D perception. We introduced an efficient hybrid architecture that integrates a full-resolution 2D tri-plane stream with a low-resolution 3D volumetric stream, fused through a lightweight integration layer for end-to-end GPU acceleration. An adaptive positional encoding is included as a lightweight auxiliary module, providing economical gains in geometric fidelity with negligible overhead. Our extensive experiments across classification, completion, segmentation, and object detection show that the method achieves substantial computational savings while mapping the efficiency–accuracy trade-off across tasks: accuracy is maintained or improved for classification and completion, while for segmentation and detection, the method trades modest accuracy for substantial efficiency gains. These results demonstrate the practical relevance of our design by enabling real-time throughput on embedded hardware, supporting its applicability to robotic perception

under resource constraints.

REFERENCES

- [1] M. Tatarchenko, A. Dosovitskiy, and T. Brox, "Octree generating networks: Efficient convolutional architectures for high-resolution 3d outputs," in *Proceedings of the IEEE international conference on computer vision*, 2017, pp. 2088–2096.
- [2] Z. Liu, H. Tang, Y. Lin, and S. Han, "Point-voxel cnn for efficient 3d deep learning," *Advances in neural information processing systems*, vol. 32, 2019.
- [3] B. Graham and L. Van der Maaten, "Submanifold sparse convolutional networks," *arXiv preprint arXiv:1706.01307*, 2017.
- [4] B. Graham, M. Engelcke, and L. Van Der Maaten, "3d semantic segmentation with submanifold sparse convolutional networks," in *Proceedings of the IEEE conference on computer vision and pattern recognition*, 2018, pp. 9224–9232.
- [5] C. Choy, J. Gwak, and S. Savarese, "4d spatio-temporal convnets: Minkowski convolutional neural networks," in *Proceedings of the IEEE/CVF conference on computer vision and pattern recognition*, 2019, pp. 3075–3084.
- [6] E. R. Chan, C. Z. Lin, M. A. Chan, K. Nagano, B. Pan, S. De Mello, O. Gallo, L. J. Guibas, J. Tremblay, S. Khamis, et al., "Efficient geometry-aware 3d generative adversarial networks," in *Proceedings of the IEEE/CVF conference on computer vision and pattern recognition*, 2022, pp. 16 123–16 133.
- [7] J. R. Shue, E. R. Chan, R. Po, Z. Ankner, J. Wu, and G. Wetzstein, "3d neural field generation using triplane diffusion," in *Proceedings of the IEEE/CVF Conference on Computer Vision and Pattern Recognition*, 2023, pp. 20 875–20 886.
- [8] J. Lee, S. Lee, C. Jo, W. Im, J. Seon, and S.-E. Yoon, "Semcity: Semantic scene generation with triplane diffusion," in *Proceedings of the IEEE/CVF conference on computer vision and pattern recognition*, 2024, pp. 28 337–28 347.
- [9] Y. Huang, W. Zheng, Y. Zhang, J. Zhou, and J. Lu, "Tri-perspective view for vision-based 3d semantic occupancy prediction," in *Proceedings of the IEEE/CVF conference on computer vision and pattern recognition*, 2023, pp. 9223–9232.
- [10] R. Liu, J. Lehman, P. Molino, F. Petroski Such, E. Frank, A. Sergeev, and J. Yosinski, "An intriguing failing of convolutional neural networks and the coordconv solution," *Advances in neural information processing systems*, vol. 31, 2018.
- [11] Y. Liu, T. Wang, X. Zhang, and J. Sun, "Petr: Position embedding transformation for multi-view 3d object detection," in *European conference on computer vision*. Springer, 2022, pp. 531–548.
- [12] Z. Wu, S. Song, A. Khosla, F. Yu, L. Zhang, X. Tang, and J. Xiao, "3d shapenets: A deep representation for volumetric shapes," in *Proceedings of the IEEE conference on computer vision and pattern recognition*, 2015, pp. 1912–1920.
- [13] A. Dai, A. X. Chang, M. Savva, M. Halber, T. Funkhouser, and M. Nießner, "ScanNet: Richly-annotated 3d reconstructions of indoor scenes," in *Proceedings of the IEEE conference on computer vision and pattern recognition*, 2017, pp. 5828–5839.
- [14] I. Armeni, O. Sener, A. R. Zamir, H. Jiang, I. Brilakis, M. Fischer, and S. Savarese, "3d semantic parsing of large-scale indoor spaces," in *Proceedings of the IEEE conference on computer vision and pattern recognition*, 2016, pp. 1534–1543.
- [15] M. Roberts, J. Ramapuram, A. Ranjan, A. Kumar, M. A. Bautista, N. Paczan, R. Webb, and J. M. Susskind, "Hypersim: A photorealistic synthetic dataset for holistic indoor scene understanding," in *Proceedings of the IEEE/CVF international conference on computer vision*, 2021, pp. 10 912–10 922.
- [16] H. Fu, B. Cai, L. Gao, L.-X. Zhang, J. Wang, C. Li, Q. Zeng, C. Sun, R. Jia, B. Zhao, et al., "3d-front: 3d furnished rooms with layouts and semantics," in *Proceedings of the IEEE/CVF International Conference on Computer Vision*, 2021, pp. 10 933–10 942.
- [17] J. Liu, Y. Chen, X. Ye, Z. Tian, X. Tan, and X. Qi, "Spatial pruned sparse convolution for efficient 3d object detection," *Advances in neural information processing systems*, vol. 35, pp. 6735–6748, 2022.
- [18] Y. Chen, J. Liu, X. Zhang, X. Qi, and J. Jia, "Voxelnext: Fully sparse voxelnet for 3d object detection and tracking," in *Proceedings of the IEEE/CVF conference on computer vision and pattern recognition*, 2023, pp. 21 674–21 683.
- [19] P. Tang, Z. Wang, G. Wang, J. Zheng, X. Ren, B. Feng, and C. Ma, "Sparseocc: Rethinking sparse latent representation for vision-based semantic occupancy prediction," in *Proceedings of the IEEE/CVF Conference on Computer Vision and Pattern Recognition*, 2024, pp. 15 035–15 044.
- [20] T. Roddick, A. Kendall, and R. Cipolla, "Orthographic feature transform for monocular 3d object detection," *arXiv preprint arXiv:1811.08188*, 2018.
- [21] A. H. Lang, S. Vora, H. Caesar, L. Zhou, J. Yang, and O. Beijbom, "Pointpillars: Fast encoders for object detection from point clouds," in *Proceedings of the IEEE/CVF conference on computer vision and pattern recognition*, 2019, pp. 12 697–12 705.
- [22] Y. Yan, Y. Mao, and B. Li, "Second: Sparsely embedded convolutional detection," *Sensors*, vol. 18, no. 10, p. 3337, 2018.
- [23] A. Milioto, I. Vizzo, J. Behley, and C. Stachniss, "Rangenet++: Fast and accurate lidar semantic segmentation," in *2019 IEEE/RSJ international conference on intelligent robots and systems (IROS)*. IEEE, 2019, pp. 4213–4220.
- [24] J. Philion and S. Fidler, "Lift, splat, shoot: Encoding images from arbitrary camera rigs by implicitly unprojecting to 3d," in *European conference on computer vision*. Springer, 2020, pp. 194–210.
- [25] Z. Li, W. Wang, H. Li, E. Xie, C. Sima, T. Lu, Q. Yu, and J. Dai, "Bev-former: learning bird's-eye-view representation from lidar-camera via spatiotemporal transformers," *IEEE Transactions on Pattern Analysis and Machine Intelligence*, 2024.
- [26] A. Vaswani, N. Shazeer, N. Parmar, J. Uszkoreit, L. Jones, A. N. Gomez, Ł. Kaiser, and I. Polosukhin, "Attention is all you need," *Advances in neural information processing systems*, vol. 30, 2017.
- [27] M. Tancik, P. Srinivasan, B. Mildenhall, S. Fridovich-Keil, N. Raghavan, U. Singhal, R. Ramamoorthi, J. Barron, and R. Ng, "Fourier features let networks learn high frequency functions in low dimensional domains," *Advances in neural information processing systems*, vol. 33, pp. 7537–7547, 2020.
- [28] B. Mildenhall, P. P. Srinivasan, M. Tancik, J. T. Barron, R. Ramamoorthi, and R. Ng, "Nerf: Representing scenes as neural radiance fields for view synthesis," *Communications of the ACM*, vol. 65, no. 1, pp. 99–106, 2021.
- [29] H. Zhao, L. Jiang, J. Jia, P. H. Torr, and V. Koltun, "Point transformer," in *Proceedings of the IEEE/CVF international conference on computer vision*, 2021, pp. 16 259–16 268.
- [30] J. Mao, Y. Xue, M. Niu, H. Bai, J. Feng, X. Liang, H. Xu, and C. Xu, "Voxel transformer for 3d object detection," in *Proceedings of the IEEE/CVF international conference on computer vision*, 2021, pp. 3164–3173.
- [31] C. Reiser, R. Szeliski, D. Verbin, P. Srinivasan, B. Mildenhall, A. Geiger, J. Barron, and P. Hedman, "Merf: Memory-efficient radiance fields for real-time view synthesis in unbounded scenes," *ACM Transactions on Graphics (TOG)*, vol. 42, no. 4, pp. 1–12, 2023.
- [32] K. He, X. Zhang, S. Ren, and J. Sun, "Deep residual learning for image recognition," in *Proceedings of the IEEE conference on computer vision and pattern recognition*, 2016, pp. 770–778.
- [33] J. Redmon, S. Divvala, R. Girshick, and A. Farhadi, "You only look once: Unified, real-time object detection," in *Proceedings of the IEEE conference on computer vision and pattern recognition*, 2016, pp. 779–788.
- [34] B. Hu, J. Huang, Y. Liu, Y.-W. Tai, and C.-K. Tang, "Nerf-rpn: A general framework for object detection in nerfs," in *Proceedings of the IEEE/CVF conference on computer vision and pattern recognition*, 2023, pp. 23 528–23 538.